Article

Carbonate electrolytes manipulate lattice oxygen dynamics of oxyhydroxides toward efficient and durable water oxidation

Le Ke [1,2], Yaping Wang [3], Xiaoyi Jiang [1], Xiude Wang[1], Kai Zhao [1], Yuyan Wan[1] & Ning Yan [1,2] ✉

Activating the lattice oxygen of catalysts can accelerate the oxygen evolution reaction. However, a fundamental understanding of the lattice oxygen dynamics remains insufficient, which ultimately impairs catalyst development. Herein, we show that a CO_3^{2-}-containing electrolyte can substantially alter the reactivity and redox stability of lattice oxygens. In particular, for CoOOH and NiCoOOH, which feature high lattice oxygen reactivity, higher degrees of CO_3^{2-} intercalation deactivate lattice oxygen, shifting the reaction pathway from the lattice oxygen mechanism to the adsorbate evolution mechanism. *Operando* spectroscopic and spectrometric analyses coupled with ^{18}O isotopic labeling corroborate the decreased metal–oxygen bond covalency and hindered lattice oxygen release caused by the intercalation of CO_3^{2-}. Importantly, the catalysts with a fine-tuned degree of CO_3^{2-} intercalation maintain high activity and stability owing to the dynamic equilibrium between lattice oxygen release and refilling, demonstrating negligible degradation in an alkaline water electrolyzer after 5000 h of operation at 0.5 A cm^{-2}. This work reveals the intricacy of lattice oxygen dynamics, offering opportunities for designing high-performance electrocatalysts for real-life applications.

Electrochemical reactions are essential for the storage and conversion of renewable energy. The anodic oxygen evolution half-reaction (OER), which plays a pivotal role in various scenarios, including green hydrogen production, CO_2 electrolysis, nitrogen fixation and electrosynthesis, is particularly important[1-4]. However, this four-proton/electron transfer process is intrinsically sluggish, which often causes high overpotential loss and impairs the energy efficiency of the device[5-7]. In many cases, a series of substeps involving multiple O-containing intermediates must take place consecutively on the catalyst surface to enable the generation of diatomic oxygen[8,9]. The activity of catalysts following such an adsorbate evolution mechanism (AEM) is heavily limited by the scaling relationship. Theoretically, the minimum overpotential (η) is ~370 mV when the binding energies of all intermediates are ideal[10,11]. This thermodynamic constraint can be overcome when

other reaction pathways are developed. For example, in the lattice oxygen-mediated mechanism (LOM), where the lattice oxygens (LOs) of catalysts participate in redox chemistry, higher intrinsic OER activity ($\eta \ll 370$ mV) is experimentally observed and well explained[12-14]. These advancements in mechanistic understanding offer compelling guidelines for the design and development of better OER catalysts.

Although high metal–oxygen bond covalency and strong hybridization of oxygen nonbonding states are believed to be descriptors of catalysts that activate the OER via LOM[15-17], the mechanistic understanding of the dynamic behavior of LOs remains inadequate. For example, rapid LO exchange during the OER often creates an amorphous catalytic surface through reconstruction, which might be heavily affected by, in addition to the intrinsic physicochemical properties of catalysts, many extrinsic factors, such as the potential

[1]School of Physics and Technology, Wuhan University, Wuhan, China. [2]Shenzhen Research Institute of Wuhan University, Shenzhen, China. [3]College of Biomass Science and Engineering & National Engineering Research Center of Clean Technology in Leather Industry & Key Laboratory of Leather Chemistry and Engineering of Ministry of Education, Sichuan University, Chengdu, China. ✉e-mail: ning.yan@whu.edu.cn

bias, pH value and ions in the electrolyte[8,18–20]. In fact, intercalated species such as PO_4^{3-} and SeO_4^{2-} have been reported to activate the lattice oxygen of oxyhydroxide OER catalysts[21,22]. This ill-defined scenario makes the establishment of a structure–LO reactivity relationship rather challenging. Discrepancies in the reaction pathways of various metal oxide and hydroxide (e.g., Co_3O_4 and NiFe hydroxide) OER catalysts are thus noted in the literature[15,23–25]. Another common challenge is associated with understanding the LO release and refilling processes during LO exchange. The governing factors that manipulate the rates of these substeps remain ambiguous. In many cases, the much faster LO release rate leads to the generation of a substantial number of oxygen defects and the sequential dissolution of adjacent metal cations, eventually causing the collapse of the crystal structure during catalysis[26–28]. Hence, state-of-the-art catalysts featuring LOM often suffer from rapid performance deterioration within 100 h, which is too far from industrial applications[27,29]. Approaches such as weakening the metal–O bond covalency by doping can indeed deactivate lattice oxygens; however, the reaction pathway is then transformed to an AEM with inherently greater polarization loss. The doping element might also dilute the active site on the surface[30–32]. Finding catalysts with ideal lattice oxygen reactivity and stability remains an uneasy task.

In this work, we show that carbonate ions, which are common anions in electrolytes, can greatly manipulate the reactivity and redox stability of LOs during the OER in classic oxyhydroxide catalysts comprising NiOOH, NiCoOOH and CoOOH. The distinct effects of adsorbed and intercalated CO_3^{2-} species are elucidated via customized electrochemical looping experiments. The dynamic behavior and mechanism of LOs in response to interfacial CO_3^{2-} are revealed by various ex situ and *operando* spectroscopic and spectrometric analyses coupled with ^{18}O-isotopic labeling. This fundamental understanding enables the rational manipulation of LO stability via CO_3^{2-} intercalation, achieving a dynamic equilibrium between LO release and refilling. The application of the fine-tuned OER catalyst in an alkaline water electrolyzer is also discussed.

Results
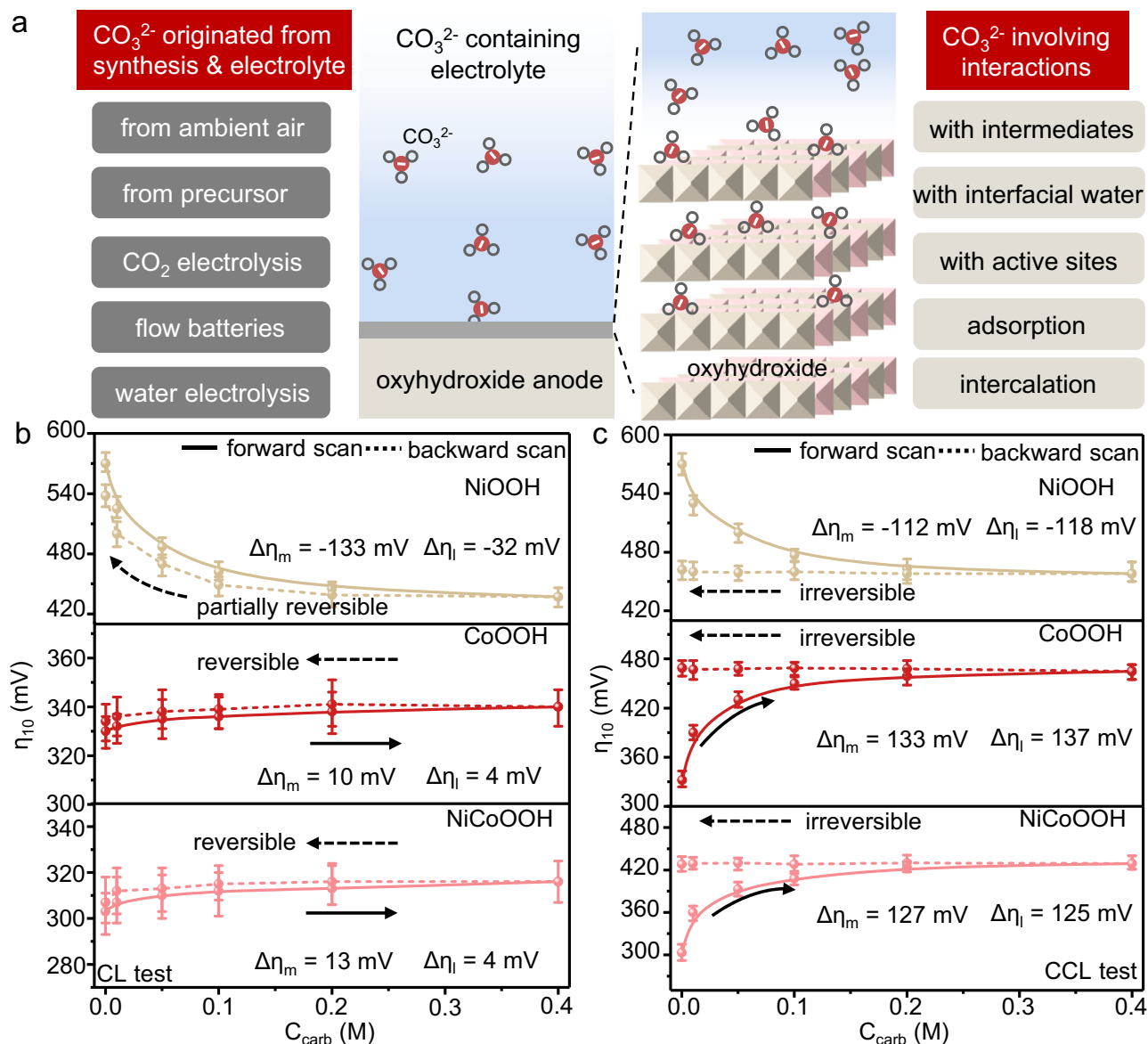
Distinct responses to carbonate ions

The possible interactions between oxyhydroxide OER catalysts and carbonate ions in the electrolyte are depicted in Fig. 1a, which might include, among others, the chemisorption of CO_3^{2-} on the surface and the intercalation of CO_3^{2-} into the interlayer spacing of the catalyst[33,34]. To probe this interfacial phenomenon, we selected three classic oxyhydroxide catalysts comprising NiOOH, CoOOH and NiCoOOH and designed a "CO_3^{2-}-looping" experiment (denoted as CL), where linear sweep voltammograms (LSVs) were sequentially recorded in 0.1 M KOH with a stepwise increase in the CO_3^{2-} concentration (0 M, 0.01 M, 0.05 M, 0.1 M, 0.2 M and 0.4 M, denoted as the "forward scan") followed by a stepwise decrease back to 0 M (denoted as the "backward scan"; see Fig. S1 for the voltammograms with/without iR correction and the experimental details in the SI). Figure 1b shows the relationship between the CO_3^{2-} concentration (C_{carb}) and the OER overpotential at 10 mA cm^{-2} (η_{10}). For NiCoOOH and CoOOH, essentially identical η_{10} values are maintained in both the forward and back scans, yet a higher C_{carb} leads to a slight increase in η_{10}. Conversely, the η_{10} of NiOOH clearly negatively correlates with C_{carb}, which decreases rapidly in the region with a low C_{carb} and then slowly stabilizes when C_{carb} reaches 0.2 M. The maximum change in η_{10} ($\Delta\eta_m$), which quantitatively shows the maximum impact on OER activity caused by the looping test, reaches 133 mV, suggesting that the introduction of CO_3^{2-} can substantially boost the OER activity. Interestingly, a hysteresis loop is observed in all plots, as η_{10} cannot be fully resumed at the designated C_{carb} in the backward scan. This results in the change in η_{10} in 0.1 M KOH measured before and after the looping test ($\Delta\eta_l$). Thus, $\Delta\eta_l$ can quantitatively reflect the electrochemical performance reversibility during the looping test.

To examine whether the lagging effect is caused by interfacial nonequilibrium, we performed a modified looping experiment, named "CO_3^{2-}-CV-looping" (denoted as CCL, see Fig. S2 for the voltammograms with/without iR correction and the experimental details in the SI), where 100 cycles of cyclic voltammetry (CVs, 0.85 - 1.77 V vs. RHE at 10 mV s^{-1}) were performed in each designated electrolyte before recording the LSVs. The new plots in Fig. 1c show substantially altered behaviors of all model catalysts compared with those in the CL test. In the forward scan, C_{carb} has a much stronger influence on the η_{10} values of CoOOH and NiCoOOH, where $\Delta\eta_m$ exceeds 133 mV and 127 mV, respectively. Its effect on NiOOH activity is similar to that observed in the CL test. In the backward scan, the change in η_{10} becomes completely irreversible, resulting in prominent hysteresis loops for all catalysts. The value of $\Delta\eta_l$ is in the range of 118–125 mV. A detailed summary of the key kinetic parameters is included in Table S1. Notably, the current density in all LSVs is normalized to the electrochemical surface area (ECSA), which does not vary significantly during both looping tests, as shown by the double-layer capacitance (C_{dl}) in Fig. S3.

To understand the contrasting catalytic behaviors of oxyhydroxides in CO_3^{2-}-containing electrolytes, we characterized the spent catalysts in detail. According to the X-ray diffraction (XRD) patterns in Fig. S4, the crystallographic structure after both the CL and CCL tests is sustained in comparison with that of the pristine sample. However, the high-resolution transmission electron microscopy (HRTEM) micrographs show expanded d-spacings along the *c*-direction for the samples after the CCL tests (see Fig. 2a–c and S5). As displayed in Fig. 2d, the average interplanar spacings for pristine CoOOH (003), NiCoOOH (006), and NiOOH (006) are 0.419 nm, 0.360 nm, and 0.340 nm, respectively, which agrees well with the literature[20,35]. After the CCL test, these d-spacings expand to 0.510 nm, 0.376 nm, and 0.367 nm, respectively. We attributed this change to the intercalation of CO_3^{2-} into the interlayer spaces. This speculation is further supported by elemental analysis via energy dispersive X-ray spectroscopy (EDX, see Fig. S6), where the elemental mappings reveal that a carbon-rich shell with a thickness of ~4 nm forms on the surface. In contrast, this carbon shell is not observed in the TEM results of CoOOH after the CL test, reconfirming that CO_3^{2-} intercalation is unlikely in this scenario (see Fig. S7).

We then obtained the X-ray photoelectron spectroscopy (XPS) depth profile of the spent catalysts after the CL and CCL tests. Figure 2e shows the segments of C 1s signals in CoOOH after the CCL test as a function of etching time. The carbonate peak, located at ~289 eV, weakens progressively with increasing depth. It completely disappears at 5200 s, which corresponds to a depth of ~5 nm (see Fig. S1). Conversely, this carbonate peak of CoOOH after the CL test disappears much earlier at 1200 s. This depth corresponds to ~1.1 nm, suggesting the presence of surface-adsorbed carbonate ions (see Figs. S9 and S10). To understand the effect of potential bias on the surface enrichment of CO_3^{2-}, we carried out *operando* surface-enhanced infrared absorption spectroscopy (SEIRAS, see Fig. S11 for experimental details)[36]. In 0.1 M KOH + 0.1 M CO_3^{2-}, the peaks at 1500 cm^{-1} and 1680 cm^{-1} correspond to the C–O and C=O stretching vibrations of interfacial CO_3^{2-}, respectively[37,38]. They intensify gradually as the potential increases from 1.22 to 1.62 V vs. RHE (see Fig. 2f and S12). Such electrosorption is also evident under potentiostatic conditions even at low CO_3^{2-} concentrations (0.5 mM), as shown in Fig. 2g and S12b. These potential-dependent characteristics are also observed in NiCoOOH and NiOOH, as shown in Fig. S13.

We thus can conclude that the anodic potential bias during the OER accelerates CO_3^{2-} electrosorption and interfacial intercalations in all oxyhydroxide catalysts. The CL and CCL tests successfully separate the influence of electrosorbed and intercalated CO_3^{2-} species on the OER activity. As shown by the CL test, the electrosorbed CO_3^{2-} species play a dominant role in manipulating the catalytic activity of NiOOH by optimizing the electronic structure of the active sites and facilitating

Fig. 1 | **Effect of carbonate-containing electrolytes on the OER activity of oxy-hydroxide catalysts. a** Schematic illustration showing the wide application of carbonate-containing electrolytes in renewable energy conversion and storage and the possible interaction of carbonate cations with the classic oxyhydroxide anode; η_{10} (the overpotential at 10 mA cm^{-2}) of 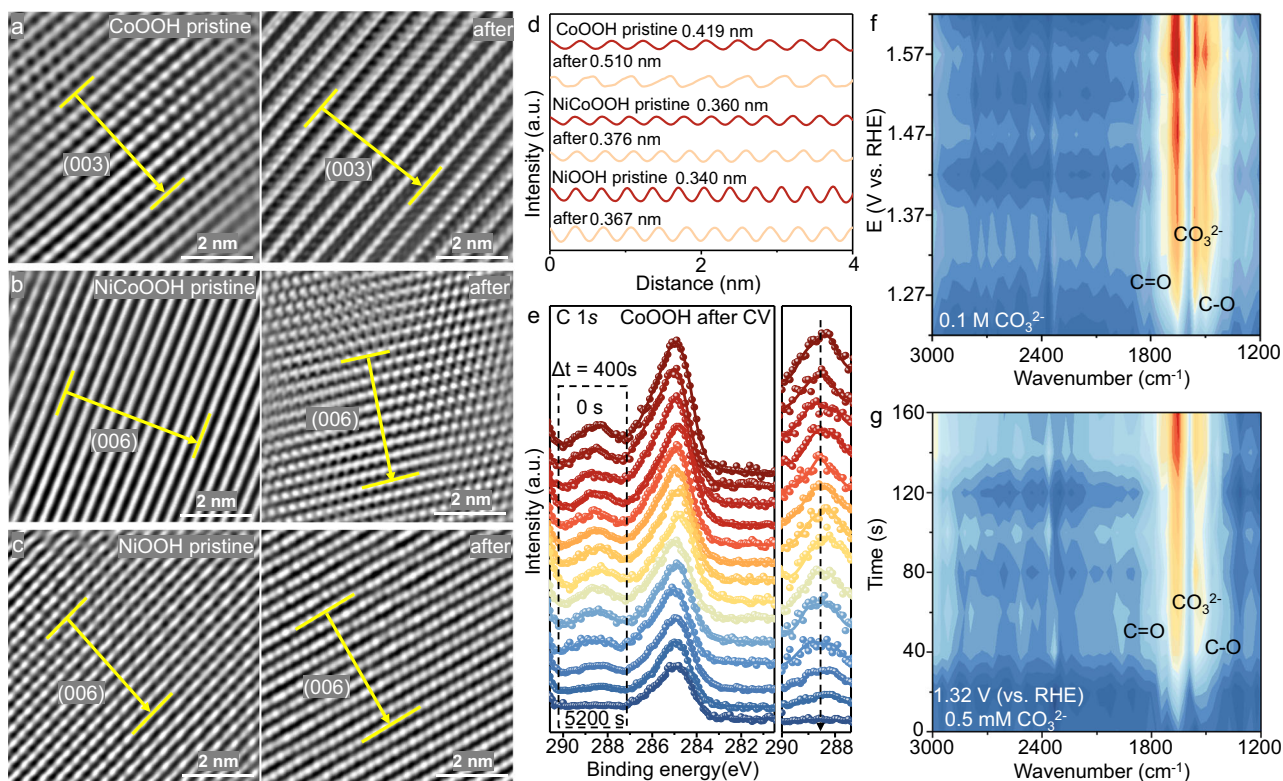classic oxyhydroxide OER catalysts in **b** "CO_3^{2-}-looping" and **c** and "CO_3^{2-}-CV-looping" tests in 0.1 M KOH solutions with varying CO_3^{2-} concentrations. All measurements were conducted at 25 °C with a scan rate of 5 mV s^{-1}. The error bars represent the standard deviations from six independent experiments.

proton transfer among the adsorbed intermediates, as documented in the literature[34,39]. These compounds have negligible effects on the activity of CoOOH or NiCoOOH. A small or no hysteresis loop is recorded, plausibly due to the reversible electrosorption–deposition of CO_3^{2-}. In comparison, in the CCL test where CO_3^{2-} intercalation occurs, a large hysteresis loop is observed since the deintercalation of CO_3^{2-} takes much time. These intercalated species thus govern the activity deterioration of CoOOH and NiCoOOH. Yet, the effects of these species on the activity of NiOOH, which is superimposed on that of the electrosorbed species, are negligible (see the summary in Table S2). This seems to contradict most findings in the literature, which show that the enlarged interlayer spacings of oxyhydroxide by intercalated CO_3^{2-} lead to enhanced OER activity due to increased surface area and/or accelerated mass transport[40,41]. This discrepancy occurs because the electrosorbed CO_3^{2-} species are also present on the surface, and the combined effect of these intercalated and adsorbed CO_3^{2-} remains strongly positive for the OER activity (*vide infra*).

Mechanistic investigations

On the basis of the conclusions above, a fundamental question arises: why do these classic oxyhydroxide OER catalysts have contrasting responses to intercalated carbonate ions? To further understand the specific behaviors among different oxyhydroxides, we created a well-defined system by preparing a series of model catalysts with increased degrees of intercalation (denoted as TMOOH-xCO$_3^{2-}$, TM is Ni, Co or NiCo). They are synthesized by soaking pristine TMOOH in 0.1 M KOH aqueous solutions containing 0.01 M CO_3^{2-}, 0.05 M CO_3^{2-}, 0.1 M CO_3^{2-} and 0.2 M CO_3^{2-}, respectively, for 24 h, as shown in Fig. 3a. The XRD patterns in Fig. S14 confirm successful and complete intercalation after the anion exchange process, as the corresponding interplanar distance increases progressively from that of the pristine samples to the most heavily intercalated samples. The bulk properties are in accordance with the surface characterization results revealed by XPS and Fourier transform infrared spectroscopy (FTIR), as shown in Figs. S15 and S16. For example, the surface concentration of carbonate (Fig. S15a),

Fig. 2 | Characterization of TMOOH after testing in a carbonate-containing electrolyte. a–c Inverse fast Fourier transform of HRTEM images of CoOOH, NiCoOOH and NiOOH before and after the CCL test; **d** interplanar distance obtained from HRTEM images; **e** segments of C 1s core-level XPS spectra as a function of etching time for CoOOH after the CCL test; *operando* SEIRAS spectra obtained in (**f**) 0.1 M KOH + 0.1 M CO_3^{2-} as a function of potential and (**g**) 0.1 M KOH + 0.5 mM CO_3^{2-} as a function of time at a constant potential of 1.32 V vs. RHE.
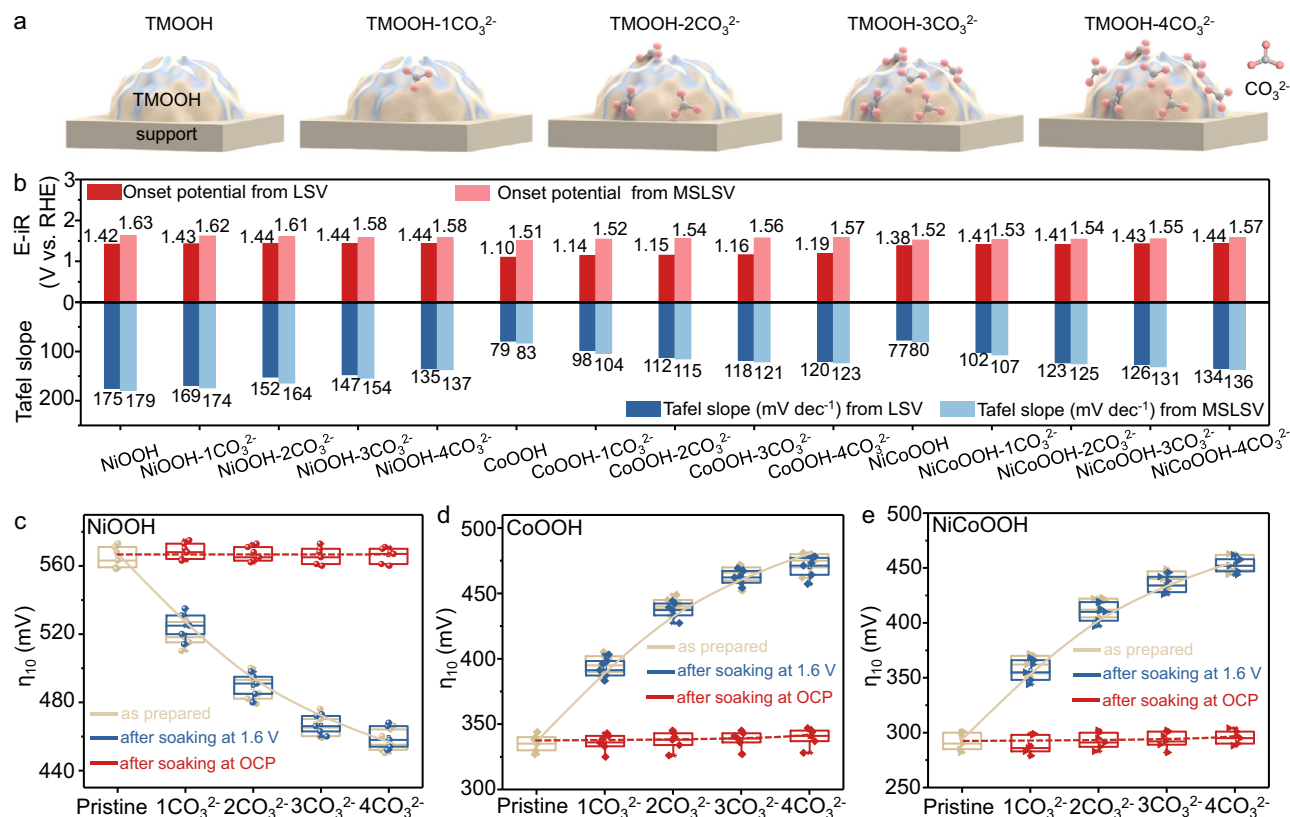
corresponding to a binding energy of ~289 eV from the deconvoluted C 1s core-level spectra, is 0%, 3.3%, 5.2%, 8.8% and 9.6% for CoOOH, CoOOH-1CO_3^{2-}, CoOOH-2CO_3^{2-}, CoOOH-3CO_3^{2-} and CoOOH-4CO_3^{2-}, respectively. The same trend is also observed for NiOOH-xCO_3^{2-} as shown in Fig. S15b. The FTIR peaks corresponding to the C-O and C = O stretching vibrations are also prominent among the model catalysts after intercalation (Fig. S16).

The OER test is performed in a purified 0.1 M KOH electrolyte without carbonate. Figure S17 compares the LSVs and Tafel slopes of various model catalysts. Owing to the potential window overlap between the OER and metal oxidation, we also used differential electrochemical mass spectrometry (DEMS) to accurately determine the onset potential and Tafel slope from the MSLSVs, as shown in Fig. 3b and S18. Notably, a higher degree of intercalation indeed worsens the OER performance of CoOOH and NiCoOOH. Compared with those of the pristine sample, the onset potential and Tafel slope of the most heavily intercalated sample increase by >100 mV and ~60 mV dec^{-1}, respectively. Conversely, the OER performance of all intercalated NiOOH catalysts is greatly improved compared with that of the pristine. This is in fact, not due to CO_3^{2-} intercalation but is attributable to the presence of surface-adsorbed CO_3^{2-} (see the FTIR spectra in Fig. S16c and the computational simulation below). Interestingly, the OER activity manipulation by the intercalated CO_3^{2-} can be fully reversible. Figures 3c–e and S19 show the recovery behaviors of model catalysts after soaking in 0.1 M KOH aqueous solution (1) with bias at 1.6 V vs. RHE for 12 h, which is fully irreversible, and (2) without bias at 1.6 V vs. RHE for 12 h, which is fully reversible. This implies that potential bias might suppress the deintercalation of CO_3^{2-}.

To explore the OER pathway, we performed ^{18}O isotopic labeling for all model catalysts and carried out *operando* DEMS studies[42,43]. The incorporation of ^{18}O isotopes into the catalyst lattice is achieved

through galvanostatic electrolysis (4 mA cm^{-2}, 12 h) in 0.1 M KOH using $H_2^{18}O$ as the solvent. The subsequent DEMS study of these labeled catalysts is carried out in 0.1 M KOH using $H_2^{16}O$ as the solvent, where the ^{18}O from the evolved diatomic oxygen can be traced to the labeled lattice oxygens. Figure 4a shows the MS signals when the catalysts are biased between 0.86 and 1.66 V vs. RHE via cyclic voltammetry. In NiOOH-xCO_3^{2-} and NiOOH, only the $^{32}O_2$ signal is recorded, suggesting the AEM pathway of the OER. Its peak intensity increases gradually with increasing degree of intercalation, which is consistent with the increased OER activity shown above. In contrast, signals of both $^{32}O_2$ and $^{34}O_2$ are recorded in the pristine and moderately intercalated Co and NiCo samples including TMOOH-1CO_3^{2-}, TMOOH-2CO_3^{2-} and TMOOH-3CO_3^{2-}, implying the presence of reactive LOs for OER catalysis[44,45]. This conclusion aligns with the pronounced pH-dependent OER activity (Figs. S20-22)[8,46,47]. The progressively decreased $^{34}O_2/^{32}O_2$ ratio and proton reaction order in Fig. 4b reflect the decrease in LO reactivity. Conversely, no $^{34}O_2$ signal is observed in TMOOH-4CO_3^{2-}, whereas the proton reaction order decreases to less than 0.37. This proves that LO is completely deactivated with the disappearance of the LOM pathway.

We also examined the dynamic behavior of TMOOH in response to CO_3^{2-}-containing electrolytes via DEMS, as shown in Fig. 4c. The ^{18}O-labeled CoOOH, NiCoOOH, and NiOOH catalysts are initially biased at 1.66 V vs. RHE in 0.1 M KOH which is sequentially changed to the ones including 0.01 M CO_3^{2-}, 0.05 M CO_3^{2-}, 0.10 M CO_3^{2-}, and 0.20 M CO_3^{2-} under *operando* conditions. The diatomic oxygen signal increases for NiOOH but decreases for CoOOH and NiCoOOH when the carbonate concentration in the electrolyte increases. This result is consistent with that obtained in the CCL test. The $^{34}O_2$ signal is only observed in CoOOH and NiCoOOH, which gradually decreases upon the introduction of CO_3^{2-}, confirming the deactivation of the lattice

Fig. 3 | OER performance of TMOOH-xCO_3^{2-}. a Schematic illustration of all TMOOH-xCO_3^{2-} model catalysts; **b** comparison of the onset potential and Tafel slope of TMOOH-xCO_3^{2-} obtained from LSV and MSLSV; **c**–**e** comparison of the η_{10} (the overpotential at 10 mA cm^{-2}) values for pristine TMOOH-xCO_3^{2-} and those after being soaked in 0.1 M KOH aqueous solution with and without bias at 1.6 V vs. RHE for 12 h. All measurements were conducted in 0.1 M KOH at 25 °C with a scan rate of 5 mV s^{-1} and a solution resistance (R_s) of 12.2 ± 0.5 Ω. Box plots display the median (centerline), the interquartile range (IQR; box bounds from the 25th to the 75th percentile), and the whiskers encompassing 1.5× IQR from the quartiles. All points outside the whiskers are defined as outliers.

oxygens. It recovers when the electrolyte is changed back to a pure 0.1 M KOH solution. This trend is further supported by the investigation of LO dynamics in different potential windows using ^{18}O-labeled model catalysts, as shown in Fig. S23a. Two model reactions were selected: the sulfite (SO_3^{2-}) oxidation reaction (SOR) features a direct chemical reaction between the oxyhydroxide and SO_3^{2-} (i.e., at the open-circuit potential), which is an ideal process for studying the chemical reactivity of LO; ethylene glycol oxidation (EGOR) occurs simultaneously with Ni^{2+}/Ni^{3+} conversion (~1.3 V vs. RHE; see Fig. S24–26 for more details), which is substantially lower than the OER potential.
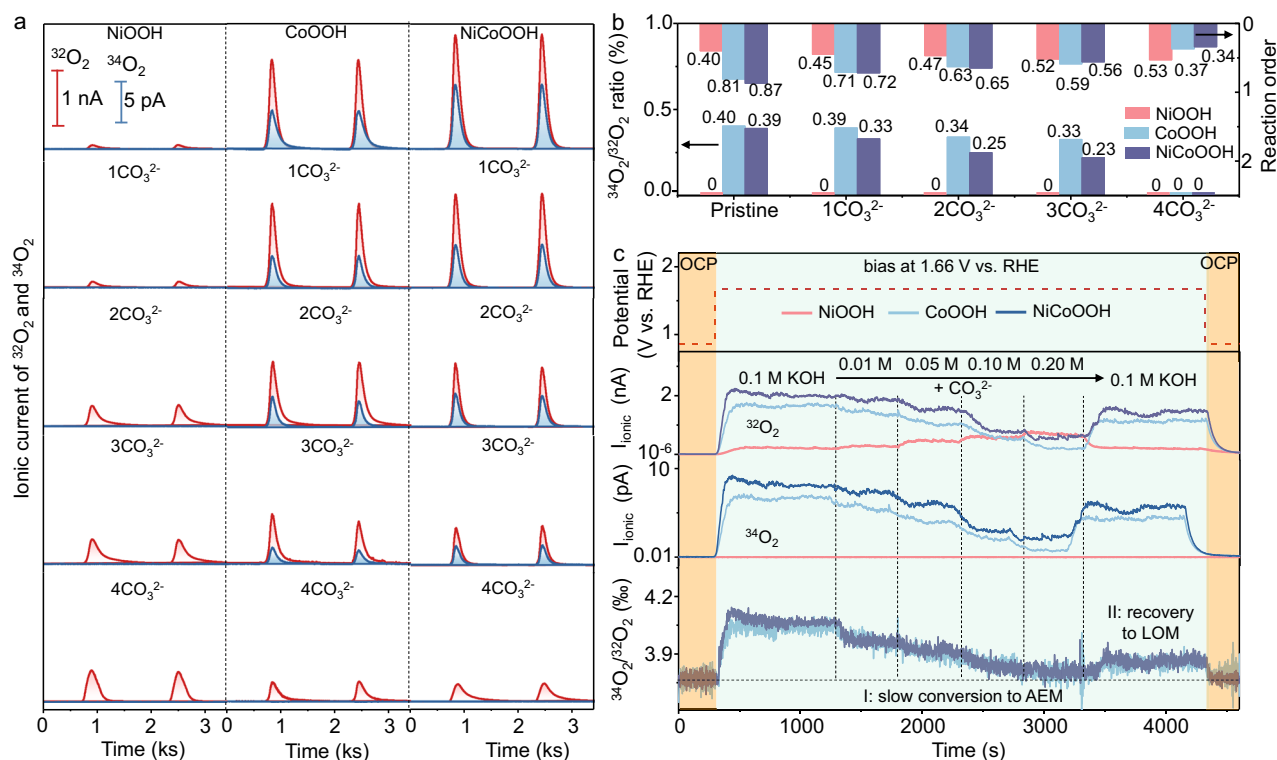
Structure–mechanism relationships and practical implications
To establish the relationship between the intercalated model catalysts and the distinctive reaction pathway evolution, we used X-ray absorption spectroscopy (XAS) to explore their electronic structure changes upon intercalation. The X-ray absorption near-edge structure (XANES) spectra of the Co and Ni K-edges, as shown in Fig. 5a, b, reveal a negative shift in the photon energy upon carbonate ion intercalation, suggesting a reduction in the average oxidation state of both Co and Ni cations. Concurrently, the increase in white line intensity after intercalation suggests a decrease in geometrical distortion of the MO$_6$ octahedron and Co/Ni 3d - O 2p orbital hybridization (M-O bond covalency)[48,49], which is in accordance with the theoretical understanding of LO reactivity[50,51].

To discern the dominant factor influencing the electronic structure change and LO reactivity, we performed a detailed analysis of the extended X-ray absorption fine structure (EXAFS) and wavelet transform (WT). The Co and Ni K-edge $k^3\chi(k)$ oscillation curves in Fig. S27

show notable peak shifts, confirming the increase in the average M–O bond length after intercalation. This is further corroborated by the Fourier transform EXAFS (FT-EXAFS) spectra and WT analysis (Fig. 5c, d). Two peaks in the FT-EXAFS spectra located at ~1.5 and ~2.5 Å are assigned to the Co-O/Ni-O and Co-Co/Ni-M bonds, respectively. A positive correlation between the Co-Co/Ni-M peak intensity and the degree of ion intercalation is observed, confirming that the CoO$_6$/NiO$_6$ in CoOOH/NiCoOOH-2CO$_3^{2-}$ is the least distorted. The fitted Co-O/Ni-O and Co-Co/Ni-M bond lengths of all the model catalysts are summarized in Fig. 5e and Tables S3 and S4. Apparently, the longer Co-O and Ni-O bond lengths in CoOOH-2CO$_3^{2-}$ and NiCoOOH-2CO$_3^{2-}$ and reduced octahedral distortion might reflect the difficulty of forming covalent bonds, pinpointing the decreased M-O covalency and eliminated LO reactivity[52,53].

On the basis of the characterization results, we established carbonate ion-intercalated TMOOH models and performed density functional theory (DFT) calculations, with a focus on the oxygen vacancy (Ov) formation energy (E$_{Ov}$), which is a key descriptor of LO reactivity[48,54,55]. The results shown in Fig. 5f indeed show that E$_{Ov}$ increases drastically upon the insertion of carbonate ions. Notably, the adsorbed carbonate ions might be also detrimental to the LO reactivity (see Fig. S28 for details). We also evaluated the M-O bond covalency of model catalysts, which can be quantified by the charge transfer energy between the unoccupied metal 3d- and occupied O 2p-band centers ($\Delta\varepsilon$)[55]. The schematic relationship between M-O covalency and LO reactivity is illustrated in Fig. S29. Pristine CoOOH and NiCoOOH have the lowest $\Delta\varepsilon$, which is consistent with the highest degree of M-O covalency and correlates with their high experimentally observed LO reactivity during the OER (see Table S5). With increasing degrees of

Fig. 4 | DEMS tests of TMOOH·xCO$_3^{2-}$. a Spectrometric signals of ^{32}O$_2$ and ^{34}O$_2$ recorded in the cyclic voltammetric scan between 0.86 and 1.66 V vs. RHE for various model catalysts in 0.1 M KOH solution with a scan rate of 1 mV s^{-1}; **b** comparison of ^{34}O$_2$/^{32}O$_2$ and proton reaction order among model catalysts;

c spectrometric signals of ^{32}O$_2$ and ^{34}O$_2$ recorded in pristine catalysts biased at 1.66 V vs. RHE; the CO$_3^{2-}$ concentration in the 0.1 M KOH electrolyte is sequentially switched from 0 M to 0.01 M, 0.05 M, 0.10 M, and 0.20 M under *operando* conditions.

intercalation, $\Delta\varepsilon$ rises up progressively, eventually leading to the diminish of LO reactivity. In contrast, the intrinsically higher $\Delta\varepsilon$ of pristine NiOOH aligns with the absence of LO reactivity. Carbonate intercalation increases $\Delta\varepsilon$ further, thereby disfavoring the activation of lattice oxygens.

We then examined the effect of CO$_3^{2-}$ intercalation on the structural change of NiOOH. The XANES data in Fig. S30 and Table S6 reveal that NiOOH undergoes similar electronic structure changes where CO$_3^{2-}$ intercalation reduces the Ni oxidation state and the degree of distortion in the NiO$_6$ octahedron. The free energy changes of the OER elementary steps via the AEM for NiOOH, CO$_3^{2-}$-adsorbed NiOOH, and CO$_3^{2-}$-intercalated NiOOH are also calculated (see Fig. S31). The deprotonation of *OH serves as the rate-determining step (RDS) for all catalysts. Both carbonate adsorption and intercalation lower the theoretical energy barrier of this step. The more substantial barrier reduction in the adsorbed model suggests that adsorbed carbonates are likely the primary contributor to the enhanced OER activity observed in NiOOH, particularly when both adsorbed and intercalated species are present[34,39].
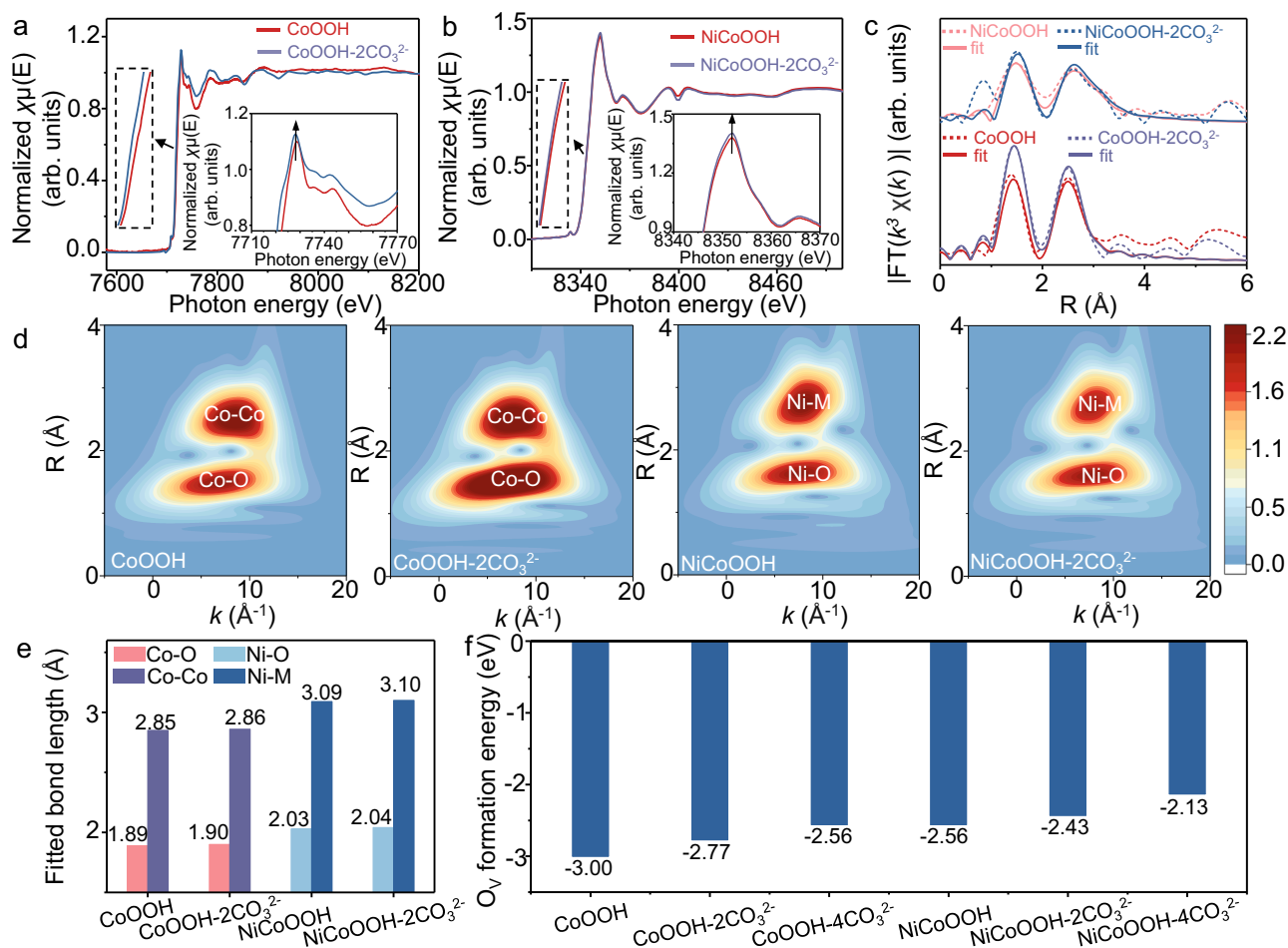
In light of the abovementioned results and analyses, the distinct impacts of carbonate ions on different types of oxyhydroxide OER catalysts are illustrated in Fig. S32. In principle, carbonate ions from the electrolyte can be easily adsorbed onto the anode surface and inserted into the interlayer spacings because of the fast ion exchange rate[35,56]. For NiOOH without reactive LO, chemisorbed CO$_3^{2-}$ is crucial for increasing OER activity. Such activity modulation is reversible once the carbonate anions are removed from the electrolyte. In contrast, for oxyhydroxides with reactive LO, there is a strong negative correlation between the OER activity and the degree of CO$_3^{2-}$ intercalation. When a sufficient number of ions are inserted, the decreased metal–oxygen bond covalency leads to suppressed LO reactivity, resulting in gradual evolution of the OER pathway from the LOM to the AEM and worsening

OER activity. This transition, together with the LO dynamics, is also fully reversible when CO$_3^{2-}$ is removed from the interlayer spacings.

Understanding such effects has strong practical implications for developing highly active yet robust OER catalysts featuring reactive LO. We examined the performance of all model catalysts under industrially relevant conditions in a zero-gap alkaline water electrolyzer (see Fig. S33)[57]. All electrolyzers show reasonable performance, as demonstrated by the polarization curves in Fig. S34. For example, at the benchmark voltage of 2 V, the electrolyzer employed with a CoOOH anode delivers a high current density of 766 mA cm^{-2}. However, their stability varies substantially under galvanostatic electrolysis at 500 mA cm^{-2} in a 6 M KOH solution, as shown in Fig. 6a. No voltage degradation is observed in either NiOOH or NiOOH·2CO$_3^{2-}$ cells. The higher activity of the NiOOH·2CO$_3^{2-}$ electrode is indeed maintained in the carbonate-free electrode under potential bias, which is in line with the model catalyst study above. Neither the CoOOH nor the NiCoOOH cell is stable, the performance of which deteriorates rapidly within 100 h. In contrast, both the CoOOH·2CO$_3^{2-}$ and NiCoOOH·2CO$_3^{2-}$ cells have low electrolysis voltages with negligible voltage decay even after 5000 h (<0.16 mV per 100 h, see Fig. 6b).

Interestingly, adding 0.2 M CO$_3^{2-}$ to the electrolyte does not affect the performance of the CoOOH·2CO$_3^{2-}$ and NiCoOOH·2CO$_3^{2-}$ electrodes, as shown in Fig. S35, suggesting that the potential bias might be beneficial in suppressing carbonate deintercalation in a pure KOH solution. A longevity test at 1 A cm^{-2} is also carried out to examine the catalyst stability at a higher anodic potential. No apparent performance degradation is observed over the testing period (see Fig. S36). The DEMS study, combined with the isotopic labeling of the spent catalysts in Fig. S37 implies that the LO reactivity is sustained. The electrocatalytic stability is also reflected by the structural integrity: the inductively coupled plasma–mass spectrometry (ICP–MS) results in Fig. S38 show the relatively low leaching rate of transition metals from

Fig. 5 | XAS spectra and Ov formation energy of the model catalysts. a, b Co and Ni K-edge XANES spectra; **c** Fourier transforms of K^3-weight Co and Ni K-edge FT-EXAFS spectra; **d** wavelet transforms for the K^3-weight Co and Ni K-edge EXAFS signals; **e** the fitting bond length data; **f** O_v (oxygen vacancy) formation energy of CoOOH and NiCoOOH with different degrees of carbonate ion intercalation.

the catalysts to the electrolyte. Thus, both CO_3^{2-}-intercalated oxyhydroxides are rather durable while featuring the LOM pathway in the OER. A detailed comparison with the literature is shown in Table S7.
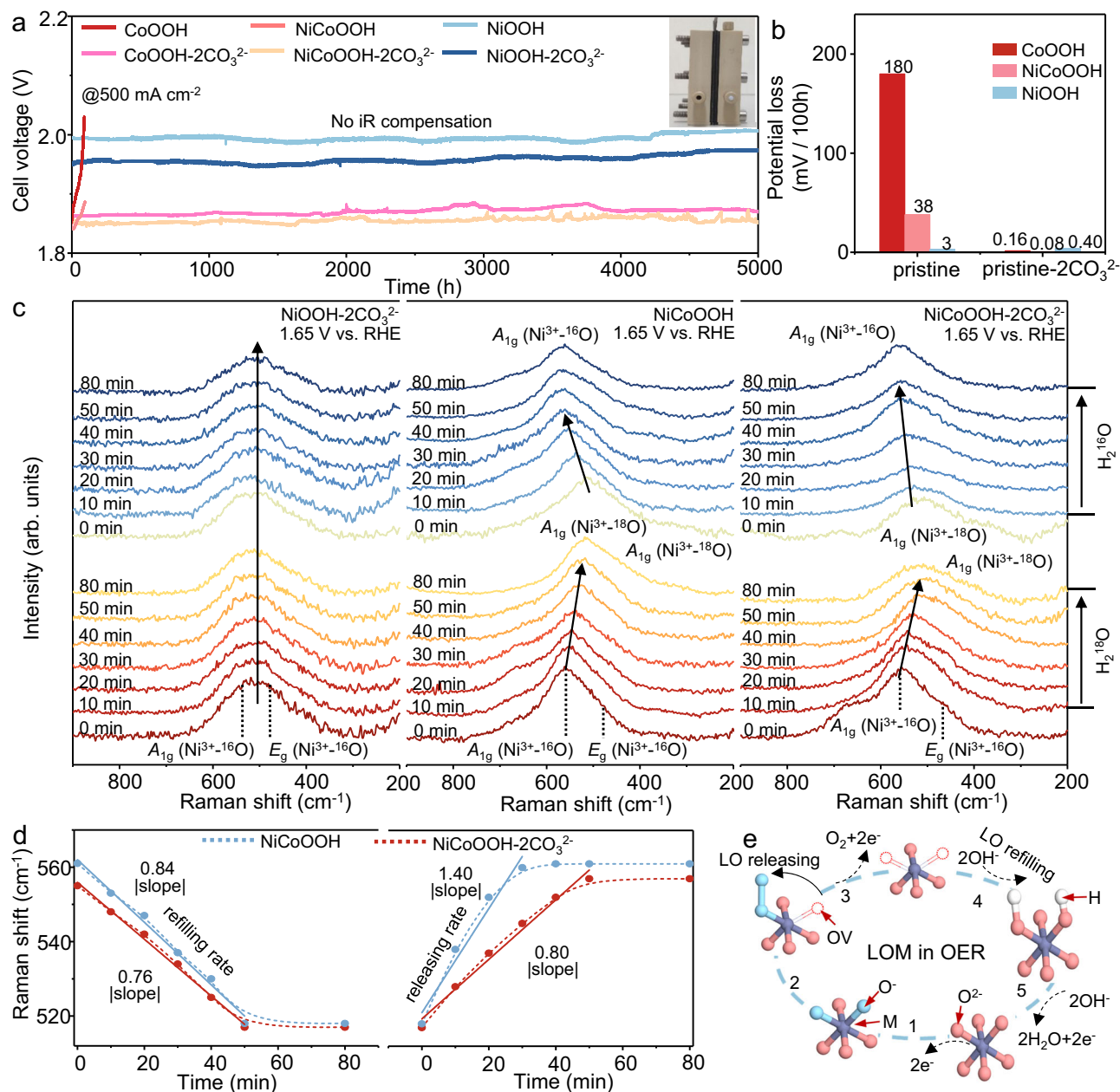
To understand the high stability of CO_3^{2-}-intercalated TMOOH with sustained LO reactivity, we designed an *operando* experiment by combining Raman spectroscopy and ^{18}O isotopic labeling to investigate the kinetics of LO release and incorporation. In the LO incorporation step, the spectrum is collected every 10 min while the catalyst is biased at a constant potential of 1.6 V vs. RHE in the $H_2^{18}O$ electrolyte. After 80 min, an identical procedure is executed to examine the LO release process while the electrolyte is replaced with $H_2^{16}O$ solution. As shown in Fig. 6c, in NiOOH, the peaks at 486 and 545 cm^{-1} correspond to E_g bending and A_{1g} stretching vibrations of Ni^{3+}-O vibrations, respectively[58,59]. It does not show any shift throughout the entire process, implying no incorporation of ^{18}O into the lattice. Conversely, the peaks of both the NiCoOOH and NiCoOOH-$2CO_3^{2-}$ catalysts clearly redshift by 38 cm^{-1} during the ^{18}O incorporation step, confirming the formation of Ni^{3+}-^{18}O bonds[60,61]. They blueshift during the ^{18}O release step, suggesting the gradual removal of lattice ^{18}O. When the ^{18}O exchange is complete, no further shift is recorded.

Therefore, the peak shift rate becomes a reasonable descriptor for evaluating the kinetics of lattice oxygen release and refilling processes. Figure 6d shows the plot of the shift in the Ni^{3+}-O A_{1g} Raman stretching vibration as a function of time for both processes. CO_3^{2-} intercalation does not significantly affect the LO incorporation rate since the absolute value of the slope in the linear region for NiCoOOH-$2CO_3^{2-}$ (0.76 cm^{-1} min^{-1}) is similar to that of NiCoOOH (0.84 cm^{-1} min^{-1}). However, the LO

release rate is greatly suppressed by CO_3^{2-} intercalation, and the slope drastically decreases from 1.40 cm^{-1} min^{-1} in NiCoOOH to 0.80 cm^{-1} min^{-1} in NiCoOOH-$2CO_3^{2-}$. This results in essentially identical LO release and refilling rates, which are beneficial for increasing the structural stability during LO exchange in catalysis. It also demonstrates that CO_3^{2-} intercalation has a stronger effect on suppressing LO release and the sequential formation of oxygen vacancies, therefore enabling the dynamic equilibrium between LO release and LO refilling (see Fig. 6e). This dynamic equilibrium effectively inhibits the net production of abundant oxygen vacancies and the sequential dissolution of metal centers. Therefore, while catalyzing the OER via the LOM pathway, NiCoOOH-$2CO_3^{2-}$ is more stable among the controls.

Discussion

In this work, we show that carbonate cations in an electrolyte can greatly affect the LO dynamics of typical oxyhydroxide catalysts during the OER. For NiOOH, which shows no LO reactivity, there is a strong positive correlation between the amount of adsorbed CO_3^{2-} and the OER activity, yet the intercalated CO_3^{2-} can hardly alter the activity. In comparison, for CoOOH and NiCoOOH, which feature high LO reactivity, the adsorbed CO_3^{2-} does not much affect the OER activity. Yet, the increasing degree of CO_3^{2-} intercalation progressively decreases the LO reactivity and OER activity, shifting the reaction pathway from the lattice oxygen mechanism to the adsorbate evolution mechanism. CO_3^{2-} intercalation offers a viable strategy for manipulating the release rate of LO during the OER, enabling the development of robust and active catalysts with sustained LO reactivity.

Fig. 6 | Stability and mechanistic study of model catalysts. a Stability test of alkaline water electrolyzers with different anode catalysts in a 6 M KOH solution at 25 °C, the inset shows the photograph of an assembled zero-gap alkaline water electrolyzer; **b** potential loss for different anode catalysts after the stability test; **c** *operando* Raman spectra of model catalysts biased at 1.6 V (vs. RHE) in 0.1 M KOH electrolyte using $H_2^{18}O$ or $H_2^{16}O$ as the solvent; **d** plots of the Ni^{3+}-O Raman peak position as a function of time during the lattice-oxygen incorporation and release steps; **e** schematic illustration of the dynamic equilibrium between the lattice-oxygen release and refilling steps caused by CO_3^{2-} intercalation during OER catalysis via the LOM pathway.

More studies should be conducted regarding the interplay between the LO and the surrounding environment to deepen the fundamental understanding. Besides, it is also likely that the synthetic procedure and storage conditions might introduce impurities to the catalysts in different ways (e.g, surface adsorption and intercalation), altering the reaction pathways via manipulating the lattice oxygen reactivity. This work offers an example that reveals the intricacy of LO dynamics, demonstrating opportunities for designing high-performance electrocatalysts for real-life applications.

Methods

Materials synthesis procedure

Materials and reagents. Chemical reagents, including $Co(NO_3)_2$, $Ni(NO_3)_2$, NaClO, KOH, K_2CO_3, Na_2SO_3, and ethylene glycol (EG), were

purchased from Shanghai Aladdin Biochemical Technology Co., Ltd. with analytical grade purity and were used without purification. The porous separator was the wet-laid nonwoven fabric offered by the NewCom energy material store. The electrolyte for each catalytic reaction was prepared by dissolving the corresponding reagents in deionized (DI) water before each measurement.

Preparation of TMOOH. We first prepared transition metal (TM, Ni, Co, and $Ni_{0.9}Co_{0.1}$) hydroxide via electrodeposition. For instance, to prepare $Co(OH)_2$, the carbon cloth, Pt plate (1 cm × 1 cm), and Hg/HgCl electrode were used as the working electrode (cathode), counter electrode, and reference electrode, respectively. The electrolyte was a 0.2 M $Co(NO_3)_2$ solution. Electrodeposition was carried out at a current density of 10 mA cm⁻² for 600 s. Then, the deposited $Co(OH)_2$ was

removed from the carbon cloth and washed with deionized water several times. To convert hydroxide to oxyhydroxide, we followed a well-established method via chemical oxidation[62,63]. Specifically, 0.1 g of Co(OH)$_2$ and 30 mL of NaClO (5 wt%) solution were added to a 50 mL Teflon-lined stainless-steel autoclave, and the pH was adjusted to 13 with a 0.1 M KOH solution. The autoclave was heated to 100 °C, which was maintained for 9 h to yield a black powder that was retrieved via centrifugation. The CoOOH powder was washed with DI water at least three times and then dried in a vacuum drying oven. The synthesis of other TMOOHs followed the same procedure.

Preparation of CO$_3^{2-}$-intercalated TMOOH. To obtain TMOOH·1CO$_3^{2-}$, TMOOH·2CO$_3^{2-}$, TMOOH·3CO$_3^{2-}$ and TMOOH·4CO$_3^{2-}$ model catalysts, pristine TMOOH powder (0.1 g) was soaked in 0.1 M KOH solutions with 0.01 M, 0.05 M, 0.10 M and 0.2 M K$_2$CO$_3$, respectively, for 12 h. The retrieved powder was washed with DI water at least three times and then dried in a vacuum drying oven.

Materials characterization

The X-ray diffraction patterns of the samples were obtained via a Cu-Kα X-ray diffractometer (XRD, Rigaku Smartlab). X-ray photoelectron spectroscopy (XPS) was performed with an ESCALab 250Xi (Thermo Scientific) spectrometer. To obtain the depth profile, Ar$^+$ sputter etching was used to remove the surface layer. Transmission electron microscopy analysis was carried out via an aberration-corrected JEM-ARM200CF microscope operated at 200 kV with a Schottky cold-field emission gun. A high-angle annular dark field (HAADF) detector and an energy-dispersive X-ray spectroscopy (EDX) detector were used to obtain dark field micrographs and elemental information, respectively. A Fourier transform infrared spectrometer (FTIR, Bruker, Invenior, 1200–4000 cm^{-1}) equipped with a liquid-nitrogen-cooled MCT (HgCdTe) detector was used to collect the FTIR spectrum. X-ray absorption spectroscopy was performed using an easyXAFS300+ spectrometer.

Procedure of operando spectroscopic and spectrometric studies

Operando surface-enhanced IR absorption spectroscopy (SEIRAS) analysis was carried out using the same FTIR spectrometer. In the homemade in situ electrochemical cell mounted on the PIKE VeeMAX III ATR accessory (see Fig. S11), the working electrode was a silicon crystal (2 cm diameter). For each experiment, the silicon crystal was polished and then coated with a gold film via electroless deposition. The catalyst was drop-casted onto the gold film via an ink containing 5 mg of catalyst, 20 μL of 5 wt% Nafion solution (DuPont), 320 μL of ethanol, and 160 μL of DI H$_2$O. The counter electrode was platinum, and the reference electrode was Hg/HgO (in 0.1 M KOH). The volume of used electrolyte was ~20 mL.

Operando Raman spectra were obtained with a confocal micro-Raman system (XploRA Plus, Horiba). All measurements were conducted with a He-Ne laser at a wavelength of 638 nm. A calibration using the silicon wafer was carried out before each experiment. The in situ electrochemical Raman experiments were carried out in a custom Raman cell (see Fig. S39), which employed a Pt wire as the counter electrode and Hg/HgO (in 0.1 M KOH) as the reference electrode. The electrolyte volume was ~5 mL.

Differential electrochemical mass spectrometry (DEMS) was carried out via a PFEIFFER QAS100 Quadrupole mass spectrometer equipped with a turbopump (HIPACE 80, PFEIFFER). The electron energy and emission current were set at 70 eV and 2000 μA, respectively. The homemade DEMS cell (see Fig. S40) contained a 40 μm-thick gold-coated porous PTFE film (porosity of 50%, pore size of 20 nm; Shanghai LingLu Instrument Corp., Ltd., China) interface that separates the aqueous electrolyte from the vacuum. The catalyst ink was drop-casted on a porous gold film, which functioned as the working electrode. A Pt wire and a Hg/HgO electrode were used as the counter electrode and reference electrode, respectively. The electrolyte volume was ~2 mL. To switch the electrolyte under operating conditions, a circulating electrolyte system was applied.

Electrochemical measurement and procedure

Basic procedures. All the electrochemical measurements were carried out with a CHI660 electrochemical workstation. In a typical three-electrode setup, a platinum plate (1 cm × 1 cm) and a Hg/HgO electrode were used as the counter electrode and reference electrode, respectively. The Hg/HgO reference electrode was calibrated against a reversible hydrogen electrode (RHE) in the same electrolyte. Briefly, a clean Pt wire was used as the working electrode in H$_2$-saturated 0.1 M KOH, and the potential at which the hydrogen oxidation/reduction current crossed zero was recorded. The potential of the Hg/HgO electrode was then calculated via the equation E(Hg/HgO) = E(RHE) - 0.926 V, and all reported potentials were adjusted accordingly. The catalyst served as the working electrode and was fabricated by drop-casting an ink onto a carbon cloth (1 cm × 1 cm). The ink was prepared by dispersing 5 mg of the catalyst in a mixture of 920 μL of ethanol, 50 μL of DI water, and 30 μL of a 5 wt% Nafion solution (DuPont). The resulting catalyst loading was 2 mg cm^{-2}. Other than specified, all electrochemical measurements were conducted at pH = 13 ± 0.1 in a 0.1 M KOH solution. In the study of the sulfite oxidation reaction (SOR), 0.1 M KOH + 0.1 M Na$_2$SO$_3$ was used as the electrolyte, yet the reaction was carried out at the open-circuit potential (OCP). For ethylene glycol oxidation (EGOR), 0.1 M KOH + 0.3 M EG was used as the electrolyte. Electrochemical impedance spectroscopy (EIS) measurements were performed at 1.46 V vs. RHE, employing a frequency range from 10^{-2} to 10^5 Hz under a sinusoidal potential perturbation with an amplitude of 5 mV. In a typical voltammetric experiment, the scan rate was 5 mV s^{-1}. Post-iR compensation was applied at 90% of the solution resistance for all reported potentials, which were converted to a reversible hydrogen electrode (RHE) via the following equation:

$$E_{RHE} = E_{Hg/HgO} + 0.0591 \times pH + 0.098 \qquad (1)$$

The electrochemical active surface area (ECSA) calculation. The ECSA was evaluated through double-layer capacitance (C$_{dl}$) measurements. First, CV scans were conducted in a non-Faradaic potential window (0.86–0.96 V vs. RHE) at 20, 40, 60, 80 and 100 mV s^{-1}. The capacitive current at a central potential was subsequently plotted as a function of the scan rate. The C$_{dl}$ was obtained from the linear fit of this plot. Finally, the ECSA was calculated via the following formula:

$$ECSA = \frac{C_{dl}}{C_s} \qquad (2)$$

where C$_s$ is the specific capacitance per unit area. The C$_s$ value is 0.040 mF cm^{-2} in this work.

The "CO$_3^{2-}$-looping" experiment (CL). In the forward scan, linear sweep voltammograms (LSVs) of pristine TMOOH were sequentially obtained in 0.1 M KOH solution with increasing carbonate ion concentrations (0 M, 0.01 M, 0.05 M, 0.10 M, 0.20 M, and 0.40 M). Then, the backward scan started immediately, where the LSVs of the same electrode were sequentially obtained in 0.1 M KOH solution with stepwise decreases in carbonate ion concentrations (0.40 M, 0.20 M, 0.10 M, 0.05 M, 0.01 M, and 0 M). The corresponding K$_2$CO$_3$ solution was used to adjust the carbonate ion concentration. For each catalyst, the CL test was conducted >6 times with the materials prepared from 3 batches. All the obtained data points were used in the plot for statistical analysis to minimize the effect caused by artifacts.

The "CO$_3^{2-}$-CV-looping" experiment (CCL). In the forward scan, linear sweep voltammograms (LSVs) of pristine TMOOH were also

sequentially obtained in 0.1 M KOH solution with increasing carbonate ion concentrations (0 M, 0.01 M, 0.05 M, 0.10 M, 0.20 M, and 0.40 M). However, before the LSV was recorded, 100 cycles of cyclic voltammetry (CV, 0.85 - 1.77 V vs. RHE at 10 mV s^{-1}) were applied to the electrode in each designated electrolyte. Then, the backward scan started immediately, where the LSVs of the same electrode were sequentially obtained in 0.1 M KOH solution with stepwise decreases in carbonate ion concentrations (0.40 M, 0.20 M, 0.10 M, 0.05 M, 0.01 M, and 0 M). Again, 100 cycles of cyclic voltammetry (CV, 0.85-1.77 V vs. RHE at 10 mV s^{-1}) were applied to the electrode in each designated electrolyte before the LSV was recorded. For each catalyst, the CL test was conducted >6 times with the materials prepared from 3 batches. All the obtained data points were used in the plot for statistical analysis to minimize the effect caused by artifacts.

Study of TMOOH-xCO$_3^{2-}$ model catalysts. LSVs of TMOOH-xCO$_3^{2-}$ model catalysts were obtained in a 0.1 M KOH solution. For the soaked samples, TMOOH-xCO$_3^{2-}$ model catalysts were first soaked in 0.1 M KOH solution with or without bias at 1.6 V vs. RHE for 12 h before the LSVs were recorded in 0.1 M KOH solution. For each catalyst, this test was conducted >6 times with the materials prepared from 3 batches. All the obtained data points were used in the plot for statistical analysis to minimize the effect caused by artifacts.

^{18}O isotopic labeling experiment. Other than specified, ^{18}O isotopic labeling of the catalyst was carried out in 0.1 M KOH electrolyte using H$_2^{18}$O (98% H$_2^{18}$O, Energy Chemical) at a constant anodic current density of 4 mA cm^{-2} for 12 h. After that, the catalysts were soaked in H$_2^{16}$O DI water for 10 min before being washed with H$_2^{16}$O DI water >3 times to remove the surface-adsorbed H$_2^{18}$O.

OER experiment. The ^{18}O-labeled catalyst was assembled into a DEMS cell and subjected to cyclic voltammetry between 0.86 and 1.66 V vs. RHE to drive the oxygen evolution reaction. The ionic current signals of the evolved oxygen species were monitored in real time by a mass spectrometer. To distinguish the signal from the natural abundance of ^{18}O, the ionic current signals of ^{34}O$_2$ and ^{32}O$_2$ were collected for both the ^{18}O-labeled and unlabeled NiCoOOH and CoOOH catalysts via DEMS. The resulting data, including the integrated area ratio of ^{34}O$_2$ to ^{32}O$_2$, are presented in Fig. S41.

SOR experiment. The ^{18}O-labeled catalysts were soaked in 0.1 M KOH + 0.1 M K$_2$SO$_3$ for 12 h with H$_2^{16}$O as the solvent to enable spontaneous SOR. No potential bias was applied in this chemical reaction. The resulting electrolyte was heated to remove all water, and the retrieved solid powder was analyzed by time-of-flight secondary ion mass spectrometry (TOF-SIMS, Tescan AMBER).

EGOR experiment. The ^{18}O-labeled catalysts were biased at a constant potential of 1.45 V (vs. RHE) in 0.1 M KOH + 0.3 M EG electrolyte for 24 h with H$_2^{16}$O as the solvent. After electrolysis, the electrolyte was concentrated and acidified with an HCl solution. Finally, the acidified solution was mixed with acetone for gas chromatography–mass spectrometry (GC–MS, Agilent 8890 GC–7000E system, USA).

Lattice oxygen incorporation and release experiments. This experiment was carried out via *operando* Raman spectroscopy. First, the ^{18}O incorporation step took place by biasing the pristine catalyst at 1.65 V vs. RHE in a 0.1 M KOH electrolyte with H$_2^{18}$O as the solvent. The spectrum was collected every 10 min. After 80 min, the electrolyte was replaced with 0.1 M KOH with H$_2^{18}$O as the solvent, and then an identical procedure was executed to obtain the Raman spectrum.

Alkaline water electrolyzer assembly and test
The alkaline water electrolyzer (AWE) used in this study features a zero-gap configuration that comprises endplates, gaskets, Ti current collectors, an anode electrode (1 cm × 1 cm), a 130 μm-thick porous separator (3 cm × 3 cm, wet-laid nonwoven fabric by polyolefin,

purchased from NewCom Energy Material Store), and a cathode electrode (see Fig. S33). Prior to use, the porous separator was immersed in a 6 M KOH solution for 48 h. Transition metal hydroxyl oxides were synthesized directly onto nickel foam (NF, 1 cm × 1 cm) as an anode via electrodeposition. TMOOH was subsequently formed under an anodic potential bias during the test. To prepare the carbonate ion-intercalated electrode, the TMOOH electrode was soaked in the designated solution for 12 h and then rinsed with DI water three times. The circulating electrolyte was a 6 M KOH solution stored in a gas-tight container. Electrolyte flow was enabled by a peristaltic pump.

Computational simulation procedure
Our density functional theory (DFT) calculation is based on the Cambridge Serial Total Energy Package (CASTEP) module. Within this framework, the electron-ion interactions were modeled with ultrasoft pseudopotentials, and the exchange-correlation effects were treated using the Perdew-Burke-Ernzerhof (PBE) formulation of the generalized gradient approximation (GGA). A plane-wave basis set with a kinetic energy cutoff of 400 eV was employed for all surface models. The Brillouin zones for the CoOOH and NiCoOOH systems were sampled at the Gamma point using a 1 × 1 × 1 k-point mesh. Structural optimizations were considered converged upon meeting the following criteria: an energy tolerance of 2.0×10^{-5} eV/atom, a maximum force of 0.05 eV/Å, a stress below 0.1 GPa, and a maximum displacement of 0.002 Å[64]. The CoOOH (110) and NiCoOOH (110) surface models with two-layer slabs were constructed on the basis of the optimized CoOOH and NiCoOOH crystal cells. The surface model was constructed with a substantial vacuum thickness of 15 Å along the non-periodic direction. This ensures that the interactions between periodic replicas of the slab are negligible. The files of the optimized computational models in CIF format are given in Supplementary Data 1.

The formation energy of an oxygen vacancy in charge state q was calculated for the CoOOH, CoOOH-CO$_3^{2-}$, NiCoOOH, and NiCoOOH-CO$_3^{2-}$ systems using the following equation:

$$E_f^v = E_T(defect : q) - (E_T(perfect) - \mu_O) + q(\varepsilon_F + E_{VBM}) \qquad (3)$$

In this equation, $E_T(defect : q)$ and $E_T(perfect)$ denote the total energies of the charged defective and pristine supercells, respectively. E_{VBM} represents the valence band maximum energy. μ_O is the oxygen chemical potential, and ε_F is the Fermi energy referenced to the E_{VBM}. We considered charge states q from 0 to +2 for the oxygen vacancy. For charged defects, a compensating background charge was applied to maintain overall supercell neutrality. To ensure consistent band alignment, the electrostatic potential of atoms in the pristine supercell was used as a reference for the defective supercell. The Fermi level ε_F was varied over the computational band gap to determine the thermodynamically stable charge state. E_{VBM} is evaluated via the following equation:

$$E_{VBM} = E_{VBM}^{perfect} + V_{aV}^{defect} - V_{aV}^{perfect} \qquad (4)$$

$$E_{VBM}^{perfect} = E_T(perfect : 0) - E_T(perfect : +2) \qquad (5)$$

where $E_{VBM}^{perfect}$ refers to the valence band maximum energy of the perfect supercell. The terms V_{aV}^{defect} and $V_{aV}^{perfect}$ correspond to the average electrostatic potentials in the defect and perfect supercell, respectively. $E_T(perfect : 0)$ and $E_T(perfect : +2)$ represent the total energies of the perfect supercell at neutral and +2 charge states, respectively.

Data availability
The data supporting the findings of this study are available within the paper and Supplementary Information file, and are also provided in the Source Data file. Other relevant data are available from the

corresponding authors upon request. Source data are provided with this paper.

References

1. McCrory, J. et al. Benchmarking hydrogen evolving reaction and oxygen evolving reaction electrocatalysts for solar water splitting devices. *J. Am. Chem. Soc.* **137**, 4347–4357 (2015).
2. Wang, X. et al. Efficient electrically powered CO_2-to-ethanol via suppression of deoxygenation. *Nat. Energy* **5**, 478–486 (2020).
3. Jiang, X. Y. et al. Integrating hydrogen utilization in CO_2 electrolysis with reduced energy loss. *Nat. Commun.* **15**, 1427–1439 (2024).
4. Leech, C. M. et al. A practical guide to electrosynthesis. *Nat. Rev. Chem.* **6**, 275–286 (2022).
5. Zhao, Z. L. et al. Boosting the oxygen evolution reaction using defect-rich ultrathin ruthenium oxide nanosheets in acidic media. *Energy Environ. Sci.* **13**, 5143–5151 (2020).
6. Song, F. et al. Transition metal oxides as electrocatalysts for the oxygen evolution reaction in alkaline solutions: an application-inspired renaissance. *J. Am. Chem. Soc.* **140**, 7748–7759 (2018).
7. Chen, D. et al. Nonstoichiometric oxides as low-cost and highly-efficient oxygen reduction/evolution catalysts for low-temperature electrochemical devices. *Chem. Rev.* **115**, 9869–9921 (2015).
8. Grimaud, A. et al. Activating lattice oxygen redox reactions in metal oxides to catalyse oxygen evolution. *Nat. Chem.* **9**, 457–465 (2017).
9. Koper, M. T. M. Theory of multiple proton-electron transfer reactions and its implications for electrocatalysis. *Chem. Sci.* **4**, 2710–2723 (2013).
10. Halck, B. N. et al. Beyond the volcano limitations in electrocatalysis - oxygen evolution reaction. *Phys. Chem. Chem. Phys.* **16**, 13682–13688 (2014).
11. Kanan, W. M. et al. In situ formation of an oxygen-evolving catalyst in neutral water containing phosphate and Co^{2+}. *Science* **321**, 1072–1075 (2008).
12. Assat, G. et al. Fundamental understanding and practical challenges of anionic redox activity in Li-ion batteries. *Nat. Energy* **3**, 373–386 (2018).
13. Aydinol, K. M. et al. Ab initio study of lithium intercalation in metal oxides and metal dichalcogenides. *Phys. Rev. B* **56**, 1354–1365 (1997).
14. Ceder, G. et al. Identification of cathode materials for lithium batteries guided by first-principles calculations. *Nature* **392**, 694–696 (1998).
15. Sun, Y. M. et al. Covalency competition dominates the water oxidation structure-activity relationship on spinel oxides. *Nat. Catal.* **3**, 554–563 (2020).
16. Hong, W. T. et al. Charge-transfer-energy-dependent oxygen evolution reaction mechanisms for perovskite oxides. *Energy Environ. Sci.* **10**, 2190–2200 (2017).
17. Hwang, J. et al. Perovskites in catalysis and electrocatalysis. *Science* **358**, 751–756 (2017).
18. Rountree, S. E. et al. Potential-dependent electrocatalytic pathways: controlling reactivity with pK_a for mechanistic investigation of a nickel-based hydrogen evolution catalyst. *J. Am. Chem. Soc.* **137**, 13371–13380 (2015).
19. Yang, C. Z. et al. Phosphate ion functionalization of perovskite surfaces for enhanced oxygen evolution reaction. *J. Phys. Chem. Lett.* **8**, 3466–3472 (2017).
20. Jia, H. N. et al. Unveiling the electrolyte cations dependent kinetics on CoOOH-catalyzed oxygen evolution reaction. *Angew. Chem. Int. Ed.* **62**, e202313886 (2023).
21. Li, Y. X. et al. Codecoration of phosphate and iron for improving oxygen evolution reaction of layered Ni(OH)₂/NiOOH. *ACS Catal.* **14**, 4807–4819 (2024).
22. Zhang, Y. J. et al. Selenate oxyanion-intercalated NiFeOOH for stable water oxidation via lattice oxygen oxidation mechanism. *J. Energy Chem.* **101**, 676–684 (2025).
23. Cai, M. M. et al. Formation and stabilization of NiOOH by introducing α-FeOOH in LDH: Composite electrocatalyst for oxygen evolution and urea oxidation reactions. *Adv. Mater.* **35**, 2209338–2209348 (2023).
24. Amin, M. A. H. et al. Role of lattice oxygen in the oxygen evolution reaction on Co_3O_4: Isotope exchange determined using a small-volume differential electrochemical mass spectrometry cell design. *Anal. Chem.* **91**, 12653–12660 (2019).
25. Zhang, N. et al. Lattice oxygen activation enabled by high-valence metal sites for enhanced water oxidation. *Nat. Commun.* **11**, 4066–4077 (2020).
26. Wu, F. Y. et al. Engineering lattice oxygen regeneration of NiFe layered double hydroxide enhances oxygen evolution catalysis durability. *Angew. Chem. Int. Ed.* **64**, e202413250 (2024).
27. Chung, Y. D. et al. Dynamic stability of active sites in hydr(oxy) oxides for the oxygen evolution reaction. *Nat. Energy* **5**, 222–230 (2020).
28. Klyukin, K. et al. Iron dissolution from goethite (α-FeOOH) surfaces in water by ab initio enhanced free-energy simulations. *J. Phys. Chem. C.* **122**, 16086–16091 (2018).
29. Sun, H. et al. Self-supported transition-metal-based electro-catalysts for hydrogen and oxygen evolution. *Adv. Mater.* **32**, 1806326 (2020).
30. Gao, T. G. et al. Switchable acidic oxygen evolution mechanisms on atomic skin of ruthenium metallene oxides. *J. Am. Chem. Soc.* **147**, 4159–4166 (2025).
31. Wu, Z. Y. et al. Non-iridium-based electrocatalyst for durable acidic oxygen evolution reaction in proton exchange membrane water electrolysis. *Nat. Mater.* **22**, 100–108 (2023).
32. Hao, S. et al. Dopants fixation of ruthenium for boosting acidic oxygen evolution stability and activity. *Nat. Commun.* **11**, 5368–5379 (2020).
33. Li, H. et al. Molecular dynamics modeling of the structures and binding energies of α-nickel hydroxides and nickel-aluminum layered double hydroxides containing various interlayer guest anions. *Chem. Mater.* **18**, 4405–4414 (2006).
34. Hunter, B. M. et al. Effect of interlayer anions on [NiFe]-LDH nanosheet water oxidation activity. *Energy Environ. Sci.* **9**, 1734–1743 (2016).
35. Yan, P. et al. Deeply reconstructed hierarchical and defective NiOOH/FeOOH nanoboxes with accelerated kinetics for the oxygen evolution reaction. *J. Mater. Chem. A* **9**, 15586–15594 (2021).
36. Li, L. J. et al. In situ investigation of interfacial water in the hydrogen evolution reaction: A comparative study unraveling the impact of oxide impurity. *ACS catal.* **14**, 15665–15674 (2024).
37. Markevich, E. et al. Very stable lithium metal stripping-plating at a high rate and high areal capacity in fluoroethylene carbonate-based organic electrolyte solution. *ACS Energy Lett.* **2**, 1321–1326 (2017).
38. Zhou, T. T. et al. Effect of fluoride on the morphology and electro-chemical property of Co_3O_4 nanostructures for hydrazine detection. *Materials* **11**, 207–223 (2018).
39. Menezes, W. P. et al. Facile access to an active γ-NiOOH electro-catalyst for durable water oxidation derived from an intermetallic nickel germanide precursor. *Angew. Chem. Int. Ed.* **133**, 4690–4697 (2020).
40. Zhang, S. M. et al. Cobalt carbonate hydroxide superstructures for oxygen evolution reactions. *Chem. Commun.* **53**, 8010–8013 (2017).
41. Zheng, T. T. et al. CoFe hydroxide nanospheres for enhanced alkaline water splitting and seawater oxidation: anion doping effects of fluorine and carbonate. *Chem. Eur. J.* **31**, e202403628 (2025).
42. Zhao, K. et al. Operando studies of electrochemical denitrogenation and its mitigation of N-doped carbon catalysts in alkaline media. *ACS catal.* **13**, 2813–2821 (2023).
43. Zhao, K. et al. Recent development and applications of differential electrochemical mass spectrometry in emerging energy conversion and storage solutions. *Chem. Soc. Rev.* **53**, 6917–6959 (2024).

44. Chen, L. et al. Unlocking lattice oxygen on selenide-derived NiCoOOH for amine electrooxidation and efficient hydrogen production. *J. Am. Chem. Soc.* **146**, 27090–27099 (2024).

45. Moysiadou, A. et al. Mechanism of oxygen evolution catalyzed by cobalt oxyhydroxide: cobalt superoxide species as a key intermediate and dioxygen release as a rate-determining step. *J. Am. Chem. Soc.* **142**, 11901–11914 (2020).

46. Wang, X. P. et al. Understanding of oxygen redox in the oxygen evolution reaction. *Adv. Mater.* **34**, 2107956–2107982 (2022).

47. Wang, L. Q. et al. Modulating the covalency of Ru-O bonds by dynamic reconstruction for efficient acidic oxygen evolution. *Nat. Commun.* **16**, 3502–3512 (2025).

48. Zhang, N. et al. Lattice oxygen redox chemistry in solid-state electrocatalysts for water oxidation. *Energy Environ. Sci.* **14**, 4647–4671 (2021).

49. Tyler Mefford, J. et al. Water electrolysis on $La_{1-x}Sr_xCoO_{3-\delta}$ perovskite electrocatalysts. *Nat. Commun.* **7**, 11053–11063 (2016).

50. Fu, Q. et al. *In Operando* synchrotron diffraction and in *Operando* X-ray absorption spectroscopy investigations of orthorhombic V_2O_5 nanowires as cathode materials for Mg-ion batteries. *J. Am. Chem. Soc.* **141**, 2305–2315 (2019).

51. Chen, M. et al. Boosting the proton intercalation via crystal plane optimization of TiS_2 for cycling-stable aqueous Zn-ion batteries. *Adv. Energy Mater.* **14**, 2400724–2400734 (2024).

52. Li, L. et al. Lanthanide-regulating Ru-O covalency optimizes acidic oxygen evolution electrocatalysis. *Nat. Commun.* **15**, 4974–4982 (2024).

53. Jensen, P. M. et al. Comparison of covalency in the complexes of trivalent actinide and lanthanide cations. *J. Am. Chem. Soc.* **124**, 9870–9877 (2019).

54. Rong, X. et al. A fundamental relationship between reaction mechanism and stability in metal oxide catalysts for oxygen evolution. *ACS Catal.* **6**, 1153–1158 (2016).

55. Song, J. J. et al. A review on fundamentals for designing oxygen evolution electrocatalysts. *Chem. Soc. Rev.* **49**, 2196–2214 (2020).

56. Liu, H.-M. et al. DFT study on MgAl-layered double hydroxides with different interlayer anions: Structure, anion exchange, host–guest interaction and basic sites. *Phys. Chem. Chem. Phys.* **22**, 2521–2529 (2020).

57. Yan, X. Y. et al. A membrane-free flow electrolyzer operating at high current density using earth-abundant catalysts for water splitting. *Nat. Commun.* **12**, 4143–4151 (2021).

58. Michael, D. J. et al. Alkaline electrolyte and Fe impurity effects on the performance and active-phase structure of NiOOH thin films for OER catalysis applications. *J. Phys. Chem. C.* **119**, 11475–11481 (2015).

59. Bo, X. et al. *Operando* Raman spectroscopy reveals Cr-induced-phase reconstruction of NiFe and CoFe oxyhydroxides for enhanced electrocatalytic water oxidation. *Chem. Mater.* **32**, 4303–4311 (2020).

60. He, Z. Y. et al. Activating lattice oxygen in NiFe-based (oxy)hydroxide for water electrolysis. *Nat. Commun.* **13**, 2191–2202 (2022).

61. Lee, S. et al. Deciphering iron-dependent activity in oxygen evolution catalyzed by nickel-iron layered double hydroxide. *Angew. Chem. Int. Ed.* **59**, 8072–8076 (2020).

62. Huang, J. H. et al. CoOOH nanosheets with high mass activity for water oxidation. *Angew. Chem. Int. Ed.* **137**, 8846–8851 (2015).

63. Kashani Motlagh, M. M. et al. Structural properties of nickel hydroxide/oxyhydroxide and oxide nanoparticles obtained by microwave-assisted oxidation technique. *Powder Technol.* **237**, 562–568 (2013).

64. Tanaka, T. et al. First-principles study on structures and energetics of intrinsic vacancies in $SrTiO_3$. *Phys. Rev. B* **68**, 205213–205220 (2003).

Author contributions

L.K. performed the material synthesis, characterization, and electrochemical tests and wrote the original manuscript. Y. W., X. J. and X. W. conducted the ToF–SIMS and GC–MS analyses. K. Z. and Y. W. assisted in the calculations. N.Y. conceived the idea, supervised the project and revised the manuscript.

Competing interests

The authors declare no competing interests.

Additional information

Supplementary information The online version contains supplementary material available at https://doi.org/10.1038/s41467-025-66076-1.

Correspondence and requests for materials should be addressed to Ning Yan.

Peer review information *Nature Communications* thanks Chan Woo Lee and the other anonymous reviewer(s) for their contribution to the peer review of this work. A peer review file is available.

Reprints and permissions information is available at http://www.nature.com/reprints

Publisher's note Springer Nature remains neutral with regard to jurisdictional claims in published maps and institutional affiliations.